Development of an optical 3D scanner based on structured light

BAKI KOYUNCU, KURTULUS KULLU
Computer Engineering Department
Ankara University
Sevket Aziz Kansu Binasi, Kat 3, A Blok, Besevler, Ankara,
TURKEY
bkoyuncu@ankara.edu.tr kkullu@eng.ankara.edu.tr

Abstract: - A 3D laser scanner based on a linear laser was constructed to obtain 3D virtual images of the objects. The scanner was adaptively organized for 3D point cloud extraction. Design and the theory of the scanner were presented together with the real life object scans. The resultant 3D virtual images of some art effects were displayed as examples.

Key-Words: - 3D Scanning, 3D Model, Point Cloud, Scanner Calibration, Structured Light, 3D Graphics

1. Introduction

3D model of an object is simply a collection of points in 3D space which represent the geometric shape of a particular object. A 3D virtual computer model can be obtained either manually by using CAD software or automatically by procedural modelling and scanning. Data obtained using a 3D scanner contains information about the shape of the object and possibly more (e.g. texture, colour, etc.) **[2]**. When the aim is to create an accurate virtual model of a real world object, then the 3D scanning becomes the best strategy **[1]**.

The aim of this work is to construct a 3D scanner such that 3D virtual models of archaeological artefacts can be created in the laboratory environment. Non-contact scanners are developed to scan these objects **[7][10]**. There are basically two non-contact active scanning techniques. These are time-of-flight and triangulation techniques.

Disadvantage of time-of-flight scanners is that they can scan an object one point at a time. As opposed to their time-of-flight counterparts, triangulation scanners can scan multiple points simultaneously by using structured light. They have limited ranges but their accuracy in short distances is relatively high.

In this study, an overview of the built scanner, based on structured light is provided. In such a scanner, the correspondence between 2D coordinates of pixels displaying the reflected light on images and distance of the object surface is the primary consideration.

2. The Scanner

The scanner consists of a revolving circular platform, a HE-NE line laser and a digital camera all of which are controlled from a standard PC. The general layout of the system can be seen in Fig. 1.

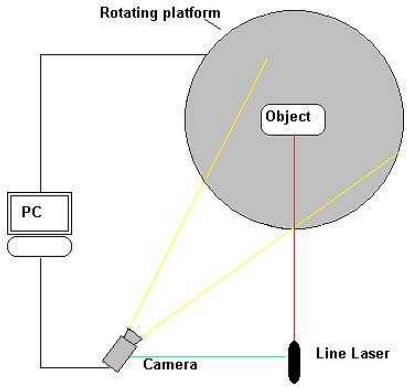

Fig. 1 Typical System block diagram (Top view)

The system covers a cylindrical scanning volume around the rotating platform of $\pi r^2 h$ where $r = 200mm$ and $h = 365mm$. The laser beam was directed vertically onto the object surface on the platform. The object was rotated around its vertical axis going through the centre of the platform. A precision stepper motor and its control mechanism rotated the platform plus the object with 360 degrees in front of the laser beam.

3. Theory

The transformation from the camera image into real world object was generated with this system. This transformation is called mapping.

When the image was captured with the camera, the 3D object is converted into 2D image on the image plane. This image will be converted into a virtual 3D image by the constructed system (scanner + PC.)

During this conversion a function, Φ, was identified for this transformation. See Fig. 2. This function, Φ, consists of structural and auxiliary parameters similar to many effecting parameters during the image capturing such as camera focal length, distances and other camera properties etc.

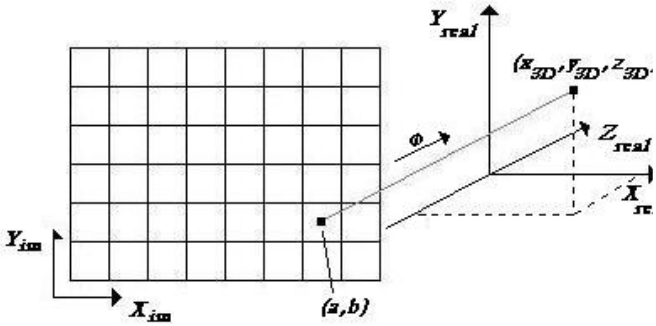

Fig. 2 A mapping ϕ from image coordinates (a, b) to virtual world coordinates (x_{3D}, y_{3D}, z_{3D}).

In mathematical terms, function Φ maps the image coordinates to virtual world coordinates as seen in **(**Fig. 2**)** and shown by the mathematical expression:

$$\Phi: \mathbb{R}^2 \rightarrow \mathbb{R}^3.$$

It was calculated by using a well known Least Square Fitting technique **(LSF) [4]**.

The origin of the world coordinates (0,0,0) was considered to be the centre point of the circular platform surface.

ϕ was considered as a 3×3 transformation matrix.

$$\Phi = \begin{pmatrix} \phi_{11} & \phi_{12} & \phi_{13} \\ \phi_{21} & \phi_{22} & \phi_{23} \\ \phi_{31} & \phi_{32} & \phi_{33} \end{pmatrix}$$

where Φ_{ij} values are the coefficients calculated by LSF and define the mapping parameters.

A point on 2D image was defined by

$$p_{im} = \begin{pmatrix} a \\ b \\ 1 \end{pmatrix}$$

and a point in 3D space was defined by

$$p_{3D} = \begin{pmatrix} x_{3D} \\ y_{3D} \\ z_{3D} \end{pmatrix}$$

Φ was multiplied by p_{im} to generate p_{3D} for every extracted point on the 2D image plane. This was shown by:

$$\Phi\, p_{im} = p_{3D} \qquad (1)$$

During the scanning, the laser is projected along the yz plane with $x = 0$. This was represented in the function Φ by the first row filled with zeros as shown here.

$$\Phi = \begin{pmatrix} 0 & 0 & 0 \\ \phi_{21} & \phi_{22} & \phi_{23} \\ \phi_{31} & \phi_{32} & \phi_{33} \end{pmatrix} \qquad (2)$$

Therefore p_{3D} which contained the 3D coordinates of the virtual object for a single scan line was calculated as:

$$p_{3D} = \begin{pmatrix} 0 \\ \phi_{21}a + \phi_{22}b + \phi_{23} \\ \phi_{31}a + \phi_{32}b + \phi_{33} \end{pmatrix} \qquad (3)$$

4. Calibration

ϕ_{ij} coefficient values were calculated by height calibration (ϕ_{2j}) along the y axis and depth calibration (ϕ_{3j}) along the z axis of the scanner system.

The depth calibration is as follows; The laser line was incident on a flat surface parallel to xy plane in front of the camera. This flat surface was placed along the z axis at 5 different locations and the image of incident laser line on each surface was recorded by the camera as shown in Fig. 3. These laser line images were identified as calibration images and later processed by using LSF technique **[4]** to give the ϕ_{3j} and z value of p_{3d}.

The height calibration was similar to depth calibration with the exception that the flat surfaces were taken in y direction parallel to xz plane.

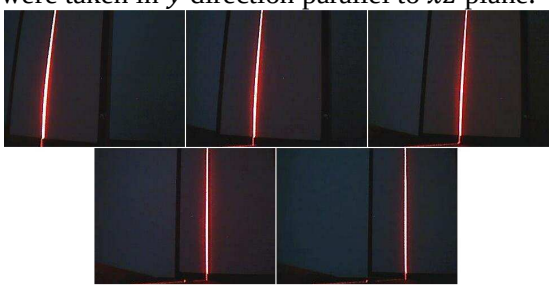

Fig. 3 Five depth calibration images of laser line recorded by the camera at 5 different locations.

There were m calibration images each of which corresponded to a depth of z_k .

z_k represented the distance of the calibration surface from the world coordinate origin and k was the index number of the calibration image.

Single calibration image contains n_k bright pixels and every bright pixel has image coordinates of (a_{lk}, b_{lk}) where $l = 1\ to\ n_k$.

The sum of squares of the difference between the calculated depth of $(\phi_{31}a_{lk} + \phi_{32}b_{lk} + \phi_{33})$ and the actual depth z_k can be written as

$$Sum = \sum_{k=1}^{m}\sum_{l=1}^{n_k}(\phi_{31}a_{lk} + \phi_{32}b_{lk} + \phi_{33} - z_k)^2$$

From **LSF** technique **[4]**, the sum will be minimal when its partial derivatives are zero with respect to ϕ_{3j}. This was shown as:

$$\frac{\partial Sum}{\partial \phi_{31}} = 2\sum_{k=1}^{m}\sum_{l=1}^{n_k} a_{lk}(\phi_{31}a_{lk} + \phi_{32}b_{lk} + \phi_{33} - z_k) = 0$$

$$\frac{\partial Sum}{\partial \phi_{32}} = 2\sum_{k=1}^{m}\sum_{l=1}^{n_k} b_{lk}(\phi_{31}a_{lk} + \phi_{32}b_{lk} + \phi_{33} - z_k) = 0$$

$$\frac{\partial Sum}{\partial \phi_{33}} = 2\sum_{k=1}^{m}\sum_{l=1}^{n_k} (\phi_{31}a_{lk} + \phi_{32}b_{lk} + \phi_{33} - z_k) = 0$$

The equations can be rearranged as shown below:

$$\phi_{31}\sum_k\sum_l a_{lk}^2 + \phi_{32}\sum_k\sum_l a_{lk}b_{lk} + \phi_{33}\sum_k\sum_l a_{lk} = \sum_k\sum_l a_{lk}z_k$$

$$\phi_{31}\sum_k\sum_l a_{lk}b_{lk} + \phi_{32}\sum_k\sum_l b_{lk}^2 + \phi_{33}\sum_k\sum_l b_{lk} = \sum_k\sum_l b_{lk}z_k$$

$$\phi_{31}\sum_k\sum_l a_{lk} + \phi_{32}\sum_k\sum_l b_{lk} + \phi_{33}\sum_k n_k = \sum_k n_k z_k$$

They can be written in matrix form as

$$\boldsymbol{M}\begin{pmatrix}\boldsymbol{\phi_{31}}\\ \boldsymbol{\phi_{32}}\\ \boldsymbol{\phi_{33}}\end{pmatrix} = \boldsymbol{Z}.$$

where

$$\boldsymbol{M} = \begin{pmatrix} \sum_k\sum_l \boldsymbol{a_{lk}^2} & \sum_k\sum_l \boldsymbol{a_{lk}b_{lk}} & \sum_k\sum_l \boldsymbol{a_{lk}} \\ \sum_k\sum_l \boldsymbol{a_{lk}b_{lk}} & \sum_k\sum_l \boldsymbol{b_{lk}^2} & \sum_k\sum_l \boldsymbol{b_{lk}} \\ \sum_k\sum_l \boldsymbol{a_{lk}} & \sum_k\sum_l \boldsymbol{b_{lk}} & \sum_k \boldsymbol{n_k} \end{pmatrix} \quad (4)$$

and

$$\boldsymbol{Z} = \begin{pmatrix} \sum_k\sum_l a_{lk}z_k \\ \sum_k\sum_l b_{lk}z_k \\ \sum_k n_k z_k \end{pmatrix} \quad (5)$$

Since $\phi_{31}, \phi_{32}, and\ \phi_{33}$ values are required to calculate the object surface depth, the above matrix equation can be rearranged as:

$$\begin{pmatrix}\boldsymbol{\phi_{31}}\\ \boldsymbol{\phi_{32}}\\ \boldsymbol{\phi_{33}}\end{pmatrix} = \boldsymbol{M^{-1}Z}$$

The inverse matrix $\boldsymbol{M^{-1}}$ and **Z** matrix can be calculated by the methods of calculus **[4]** and finally $\phi_{31}, \phi_{32}, \phi_{33}$ values can be derived as:

$$\boldsymbol{\phi_{31}} = \left(\left(\sum_k \boldsymbol{n_k}\sum_k\sum_l \boldsymbol{b_{lk}^2} - \left(\sum_k\sum_l \boldsymbol{b_{lk}}\right)^2\right)\sum_k\sum_l \boldsymbol{a_{lk}z_k} + \left(\sum_k\sum_l \boldsymbol{a_{lk}}\sum_k\sum_l \boldsymbol{b_{lk}} - \sum_k \boldsymbol{n_k}\sum_l \boldsymbol{a_{lk}b_{lk}}\right)\sum_k\sum_l \boldsymbol{b_{lk}z_k} + \left(\sum_k\sum_l \boldsymbol{b_{lk}}\sum_k\sum_l \boldsymbol{a_{lk}b_{lk}} - \sum_k\sum_l \boldsymbol{a_{lk}}\sum_k\sum_l \boldsymbol{b_{lk}^2}\right)\sum_k \boldsymbol{n_k z_k}\right) / |\boldsymbol{M}|$$

$$\boldsymbol{\phi_{32}} = \left(\left(\sum_k\sum_l \boldsymbol{a_{lk}}\sum_k\sum_l \boldsymbol{b_{lk}} - \sum_k \boldsymbol{n_k}\sum_l \boldsymbol{a_{lk}b_{lk}}\right)\sum_k\sum_l \boldsymbol{a_{lk}z_k} + \left(\sum_k \boldsymbol{n_k}\sum_k\sum_l \boldsymbol{a_{lk}^2} - \left(\sum_k\sum_l \boldsymbol{a_{lk}}\right)^2\right)\sum_k\sum_l \boldsymbol{b_{lk}z_k} + \left(\sum_k\sum_l \boldsymbol{a_{lk}}\sum_k\sum_l \boldsymbol{a_{lk}b_{lk}} - \sum_k\sum_l \boldsymbol{b_{lk}}\sum_k\sum_l \boldsymbol{a_{lk}^2}\right)\sum_k \boldsymbol{n_k z_k}\right) / |\boldsymbol{M}|$$

$$\boldsymbol{\phi_{33}} = \left(\left(\sum_k\sum_l \boldsymbol{b_{lk}}\sum_k\sum_l \boldsymbol{a_{lk}b_{lk}} - \sum_k\sum_l \boldsymbol{a_{lk}}\sum_k\sum_l \boldsymbol{b_{lk}^2}\right)\sum_k\sum_l \boldsymbol{a_{lk}z_k} + \left(\sum_k\sum_l \boldsymbol{a_{lk}}\sum_k\sum_l \boldsymbol{a_{lk}b_{lk}} - \sum_k\sum_l \boldsymbol{b_{lk}}\sum_k\sum_l \boldsymbol{a_{lk}^2}\right)\sum_k\sum_l \boldsymbol{b_{lk}z_k} + \left(\sum_k\sum_l \boldsymbol{a_{lk}^2}\sum_k\sum_l \boldsymbol{b_{lk}^2} - \left(\sum_k\sum_l \boldsymbol{a_{lk}b_{lk}}\right)^2\right)\sum_k \boldsymbol{n_k z_k}\right) / |\boldsymbol{M}|$$

where $|\boldsymbol{M}|$ stands for the determinant of $\boldsymbol{M}$.

A quantitative view can be derived from the following example with 5 calibration images (m=5) for depth measurements. A set of five bright pixels from each calibration image were considered and presented as:

$\mathbf{1}.\boldsymbol{image} = \{(4,3),(5,4),(5,20),(6,58),(7,70)\}$

$\mathbf{2}.\boldsymbol{image} = \{(12,4),(12,5),(13,7),(13,18),(15,30)\}$

$\mathbf{3}.\boldsymbol{image} = \{(33,5),(34,13),(36,75),(37,88),(37,90)\}$

$\mathbf{4}.\boldsymbol{image} = \{(42,95),(45,82),(47,18),(48,8),(49,6)\}$

$\mathbf{5}.\boldsymbol{image} = \{(60,70),(61,54),(61,66),(66,28),(68,8)\}$

The depth distances, $(\boldsymbol{z_k})$, between the 5 calibration surfaces and the world coordinate origin are measured as -20cm -10cm, 0cm, 10cm and 20cm respectively .

Using these example 2D calibration image points and their respective depth information, the elements of matrices $\boldsymbol{M}$ and $\boldsymbol{Z}$ in Equations **(4)** and **(5)** were calculated. The results were substituted in $\phi_{31}, \phi_{32}, \phi_{33}$ equations to obtain their numerical values for depth calibration as shown below:

$$\boldsymbol{\phi_{31}} = 0.6573$$
$$\boldsymbol{\phi_{32}} = -0.0075$$
$$\boldsymbol{\phi_{33}} = -21.1778$$

$\phi_{21}, \phi_{22}, \phi_{23}$ coefficients were again calculated similarly for the height calibration images.

These values, generated during the calibration, were placed in Equation **(3)** to calculate the and coordinates of the virtual object surface points with along a single laser scan line.

5. Generation of Object Point Cloud

Once the camera and the laser positions were fixed, the calibration was carried out and the mapping function in Equation 3.2 was generated.

The platform was rotated with a step angle of by a stepper motor control. An image of the laser line on the object surface was taken by the camera at every rotational step and identified as object image.

The mapping function was multiplied with the bright pixel coordinates of the object image and, as a result, virtual 3D coordinates of the object surface for one laser line was produced (See Equation **(1)**).

These 3D coordinates of the object surface along the laser line were rotated around axis and the axis value was introduced at every step.

This rotation effect was introduced by multiplying the virtual 3D coordinates with the rotational matrix shown here:

i = number of rotations (i=0 to 399).

The rotational procedure was continued and a cloud of virtual 3D coordinates were obtained for the whole object surface.

Scanning process was performed in a dark room where only the reflected laser light from the object surface was visible as shown in Fig. 4. 2D pixel positions of the single bright pixels on the captured image must be defined in order to generate virtual 3D model of the object.

Fig. 4 An example scan image

Captured image of the laser line had a contour with a finite width of more than one pixel. This finite width was reduced to one-pixel wide contour by using a technique called *thinning* in image processing **[5].** This technique *was applied* many times on the captured image so that one-pixel wide laser light contour was obtained.

6. Results

A few example objects were scanned and their corresponding point clouds were generated as shown in Fig. 5.

For comparison purposes, basic dimensional parame- ters were measured from the acquired point clouds representing the virtual objects and the real objects. These values were presented in **Table 1**.

These results were obtained with 5 calibration images along z axis and 5 calibration images along y axis.

		Real object (cm)	Virtual object (cm)	Relative error
Conic vase	Radius	8.15	8.45726	0.0377
	Height	36.6	37.94335	0.0367
Pen holder	Base side	6.5	6.71759	0.0335
	Height	15	15.49953	0.0333
Kettle	Base narrow r	6.3	6.51421	0.034
	Base wide r	8.1	8.42003	0.0395
	Height	23	23.87275	0.0379
Jug	Widest r	6.9	7.12828	0.0331
	Height	13.6	14.08976	0.036

Table 1: Examples of dimensions for both real objects and acquired clouds

The relative errors were calculated as (virtual object measurement - real object measurement) / real object measurement.

Fig. 5 Scanned objects and corresponding point clouds.

For example, the relative error for the conic vase radius was:

$$relative\ error = \frac{8.45726 - 8.15}{8.15} \cong 0.0377$$
$$= \%3.77$$

The average relative error for the scanner system was calculated from Table 1 as

$$\bar{e} = \%3.57$$

This average relative error was introduced to every virtual 3D coordinate in each point cloud. But this error was considered small and did not affect the reconstructed object shape to the naked eye.

7. Conclusions

A computer controlled 3D linear laser scanner based on line laser light was developed in this study. Real 3D small size objects were scanned by using this scanner. Initially their 2D images and later on their 3D virtual computer images were realized by introducing various software techniques.

Single camera was used to capture the laser line images on the object surface. These images were calibrated to develop the 3D virtual image of the object on the computer monitor. The capture of the laser line image was not precise due to object surface topography. This resulted in a %3.5 average error deviation of the object shape in the virtual object.

It is a well known fact that LSF estimation becomes more accurate as the number of sample points increases **[4]**. Hence, one way to increase the accuracy would be to increase the number of calibration images.

During the project the focus was on automation, efficiency and ability to deal with external interferences. 3D point cloud generation from the scanner is presented here as the first step in the targeted fully automated scanning system.

References:

[1] F. Bernardini and H. Rushmeier. The 3D Model Acquisition Pipeline . *Computer Graphics Forum* . 2002 .

[2] Brian Curless. From Range Scans to 3D Models. *Computer Graphics*. November 1999, Vol. 33, 4.

[3] B. Curless and M. Levoy. Better optical triangulation through spacetime analysis. In *ICCV '95: Proc. 5th International Conf. on Computer Vision*, page 987, Wahington, DC, USA, 1995. IEEE Computer Society.

[4] F.R. Giordanov, M.D. Weir, W.P. Fox. A First Course in Mathematical Modeling. *Thomson Brooks/Cole*, 2003.

[5] R.C. Gonzales, R.E. Woods. Digital Image Processing. *Prentice Hall – Pearson*, 2002.

[6] R.I. Hartley and P. Sturm. Triangulation. *Computer Vision and Image Understanding*, vol. 68, pp. 146-157, 1997.

[7] M. Levoy, et al. The Digital Michelangelo Project: 3D Scanning of Large Statues. *Proc. 27th annual conference on computer graphics and interactive techniques*. 2000. pp. 131-144.

[8] X. Q. Meng and Z. Y. Hu. A new easy camera calibration technique based on circular points. *Pattern Recognition*. 36(5): 1155-1164, 2003.

[9] B. Triggs, P. McLauchlan. Bundle Adjustment – A Modern Synthesis. In *Vision Algorithms: Theory and Practice*, LNCS, pp.298-375. Springer Verlag, 2000.

[10] İ. Yıldırım, B. Demir, S. Ertürk. E-Devlet İçin Kültür Varlıklarının 3-Boyutlu Modellenmesi ve Gösterimi. *14. IEEE Sinyal İşleme ve İletişim Uygulamaları Kurultayı (SIU' 2006)*. 2006.

[11] Z. Zhang. A flexible new technique for camera calibration. *IEEE trans. Pattern Analysis and Machine Intelligence*, 22(11):1330-1334, 2000.